A Retinex-Based Variational Model for Enhancement and Restoration of Low-Contrast Remote-Sensed Images Corrupted by Shot Noise

I. P. Febin, *Student Member, IEEE*, P. Jidesh, *Senior Member, IEEE*, and A. A. Bini

***Abstract*—Remotely sensed images are widely used in many imaging applications. Images captured under adverse atmospheric conditions lead to degraded images that are contrast deficient and noisy. This study is intended to address these defects of remotely sensed data efficiently. A perceptually inspired variational model is designed based upon the Bayesian framework, powered by the retinex theory. The atmospheric noise or the shot noise (precisely following a Poisson distribution) and contrast inhomogeneity are addressed in this article. The model thus designed is tested and verified both visually and quantitatively using various test data under different statistical measures. The comparative study reveals the efficiency of the model.**

***Index Terms*—Contrast enhancement, denoising, perceptual image processing, variational method.**

I. Introduction

MONITORING of natural phenomena, mapping of land cover, meteorological studies, military surveillance, etc. actively use remote sensing images to give real-time updates. In remote sensing, the sensors kept on aircraft or satellites measure the electromagnetic radiations getting reflected and scattered from different objects on earth to study about them. Based on the platform of use it can be categorized as airborne and space-borne remote sensing. Airborne imagery generally uses spacecrafts for capturing the aerial images whereas space-borne technique makes use of satellites to capture overhead images of different locations on earth continuously.

Remote sensing images generally get degraded due to the interaction with atmospheric particles and end up forming low-contrast and noisy images. These degradations limit the different applications of these data eventually by reducing the accuracy and precision. As the images captured (e.g., aerial, hyperspectral, multispectral, Radar, etc.) are severely degraded due to intensity inhomogeneity across the region of the capture, image enhancement is an inevitable preprocessing step in most of the remote-sensed imaging applications. The major degradation scenario can be attributed to the environmental conditions which reduce the contrast and the details of the captured remote sensing images [1].

Contrast enhancement is generally processed in a linear or nonlinear manner. The spatial domain enhancement strategies are pioneered by the linear contrast stretching methods that change the range of intensity values. Histogram equalization (HE) is another widely used technique which tries to equalize the density of the pixel values [2]. Nevertheless, these methods lead to overenhancement to the high peaks in the input data. This issue is addressed to a considerable extent in brightness-preserving dynamic HE [3] and histogram modification framework [4]. Yet another spatial domain model has been proposed for contrast enhancement. This model uses an adaptive gamma correction with weighting distribution (AGCWD) [5]. Nevertheless, they tend to neglect the local image features while considering the global aspect of the data.

The fact discussed above has opened up an era of transformed domain techniques such as singular value decomposition (SVD)-based model [6], discrete cosine transform (DCT)-based model [7], etc. In [6], a singular value equalization method is proposed to adjust the image brightness. A discrete wavelet-based alternative is provided in [1] which is claimed to achieve a better contrast enhancement. A method using discrete wavelet transform (DWT) and adaptive intensity transformation is also introduced for remote-sensed image enhancement in [9]. However, the method is highly sensitive to the set parameters which are practically difficult to choose adaptively. Further to mention, a retinex-based multiscale method and a general illumination normalization method is proposed in [10] and [11], respectively, for optical and multiple remote-sensed images. However, as noted earlier, these methods also fail to retain the local features in the image, though they yield good enhancement results as far as global features are concerned.

The local feature enhancement has been considered in a transformed domain model proposed in [7], where the authors propose a global enhancement using a modified histogram formation. A DCT is employed in this model to preserve the local features properly. A further improvement can be noticed in the work [8], where the authors propose a histogram compacting transform along with a linear stretch to enhance the contrast of remote-sensed data. A local remapping algorithm is included in this model to preserve more details in the course of linear stretching.

Manuscript received May 6, 2019; revised October 9, 2019, December 7, 2019, and January 23, 2020; accepted February 15, 2020. Date of publication February 27, 2020; date of current version March 17, 2020. The work of I. P. Febin and P. Jidesh was supported by the Science and Engineering Research Board, India, under the Project Grant ECR/2017/000230. *(Corresponding author: P. Jidesh.)*

I. P. Febin and P. Jidesh are with the Department of Mathematical and Computational Sciences, National Institute of Technology Karnataka, Surathkal 575025, India (e-mail: febimolu@gmail.com; jidesh@nitk.edu.in).

A. A. Bini is with the Indian Institute of Information Technology, Kottayam 686635, India (e-mail: biniaa@gmail.com).

Digital Object Identifier 10.1109/JSTARS.2020.2975044

Along with the contrast related artifacts, many aerial and satellite data are contaminated by the unavoidable noise intervention either during their capture or transmission. Generally, noises present in such images can be categorized as data-independent thermal noise, stripping noise, and data-dependent shot noise (Poisson noise) [12]. Removal of data-correlated noise, such as shot noise, is comparatively more challenging than the common data-independent counterparts. Though there are many models proposed for denoising the data and enhancing the contrast, a handful of them perform both simultaneously. In this article, we intend to address the problem of enhancing and denoising the data simultaneously. A perceptual model based on the retinex theory has been employed to perform these intended tasks. The variational framework being an effective strategy to solve the inverse problems and analyze them from a theoretical perspective, we resolve to explore a variational retinex framework based on the perceptual model for enhancing and restoring images.

II. Retinex Theory

Human visual system perceives the color of an object equally in all lighting variations, this illusion is known as the Retinex effect [17]. According to Retinex theory, the intensity of an image can be represented as the product of its illumination and reflectance, i.e.,

$$I(x,y) = L(x,y)R(x,y) \tag{1}$$

where $I(x,y)$ represents the digitized intensity image of size $M \times N$, $R(x,y)$ and $L(x,y)$ represent the digitized reflectance and illumination of the image, respectively. Initially, retinex was proposed as a random walk algorithm by Land and McCann [13]–[15]. Based on the study of Land *et al.* (refer [14]) most of the retinex methods perform a logarithmic conversion. In a logarithmic domain, it can represented as

$$i = l + r \tag{2}$$

where $i = \log(I),\ l = \log(L)$, and $r = \log(R)$. Here, computation also is less complex. A variational framework for Retinex was first proposed by Kimmel *et al.* in [16]. It is based on the assumption that the illumination is spatially smooth. The model amounts to

$$\min E[l] = \int_\Omega \left(\|\nabla l\|_2^2 + \alpha (l-i)^2 + \beta \|\nabla (l-i)\|_2^2 \right) dxdy. \tag{3}$$

However, as observed in many previous works, the reflectance is piecewise constant and based on this, a new total variation (TV)-based retinex framework has been introduced in [17]. The authors of this work assume that the reflectance belongs to a space of bounded variation (BV) in which the TVs are bounded. Their proposed optimization functional includes both illumination and reflectance terms. They have also suggested the use of advanced numerical algorithms for fast computation. The functional of this model takes the form

$$\min E[l,r] = \int_\Omega \|\nabla r\| dxdy + \alpha \int_\Omega \|\nabla l\|_2^2 dxdy + \beta (l+r-i)^2 dxdy + \mu \int_\Omega l^2 dxdy. \tag{4}$$

A nonlocal TV model for retinex is also introduced by Zosso *et al.* [18]. In [19], Li *et al.* proposed the use of a variational framework for retinex in remote sensing images to address the low-contrast issues. The first term in the expression is based on the assumption that illumination is spatially smooth. It denotes the L^2 norm of the illumination, and minimizing the L^2 norm reduces the inhomogeneity in the data. The second term minimizes the adaptive TV norm of the reflectance. Reflectance being the property of the object on which the light falls, it is assumed to be spatially nonsmooth so as to retain the edges and other frequent intensity variations. The last term is the fidelity term for reflectance. Here, the authors used the same piecewise constancy assumption on the reflectance. However, instead of applying TV prior, in all cases they used a combination of both TV and L^2 norm priors according to the edge extraction result. The model is represented as

$$\min E[r] = \int_\Omega \|\nabla (r-i)\|_2^2 dxdy + \lambda_1 \int_\Omega (\|\nabla r_t\|_t^t) dxdy + \lambda_2 \int_\Omega (exp(r) - 1/2)^2 dxdy \tag{5}$$

where t changes value between one and two based on whether the pixel belongs to an edge or not.

Later, a spatially adaptive retinex variational model was also introduced to apply in the remote sensing domain [20], where they proposed the usage of a weight parameter W to regulate the TV prior, and a fast numerical implementation has been performed to improve the computational efficiency. The modified functional appears

$$\min E[r] = \int_\Omega \|(i-l-r)\|^2 dxdy + \lambda_1 \int_\Omega (\|\nabla l\|_2^2) dxdy + \lambda_2\, W \int_\Omega (\|\nabla r\|) dxdy + \lambda_3 \int_\Omega (exp(r) - 1/2)^2 dxdy. \tag{6}$$

Even though these methods could enhance the remote-sensed images to a considerable extent, they tend to ignore the inherent noise present in these images. Hence, after the enhancement, noise appears more prominent in the results.

III. Proposed Retinex Model

In the proposed method, it is assumed that the illumination l is spatially smooth and to enforce this, the L_2 norm of the illumination is being used in the formulation of the functional. Further, the reflectance and intensity variations are represented using the nonlocal framework to ensure the coarse operations on textured areas and boundaries to actively enforce the piecewise smooth assumption (refer [21]). A weight matrix $W(x)$ is also used to scale the TV norm according to the magnitude of the gradient. This weight function helps to retain more details on the edges and at the same time, it helps in smoothing out the homogeneous intensity regions. The weight function is defined as

$$W(x) = 1 + \frac{1}{1 + \|\nabla x\|}. \tag{7}$$

The Weberized TV restoration proposed by Shen *et al.* [22] stated the influence of background in perceiving the change in the intensity. According to this vision psychology, a Weberized TV model has been successfully introduced for restoration [22]. Hence, a Weberized TV regularization has been employed in the present study to enhance the visual appearance of the restored data. The reflectance R is constrained using $(R-1/2)^2$ which forces the reflectance R to be close to $1/2$ or the trivial average of the reflectance, assuming this range to be $[0-1]$. Converting this constrain in a logarithmic domain gives $(\exp(r)-1/2)^2$. Minimization of the term $(r-i+l)$ enforces the condition $i=l+r$. The data fidelity $(I-I_0\log(I))^2$ assuming a shot noise following the Poisson distribution has been derived in this proposed study using the maximum *a posteriori* (MAP) estimation of the noise probability density function (PDF). The details may be found in Appendix A. The proposed functional for enhancement and restoration is shown as follows:

$$\begin{aligned}\min_{l,r,i}\{E(l,r,i)\} = &\int_\Omega \|\nabla l\|_2^2 dxdy + \lambda_1\int_\Omega W(r)\|\nabla\hat{r}\|dxdy\\ &+\lambda_2\int_\Omega(\exp(r)-1/2)^2dxdy\\ &+\lambda_3\int_\Omega W(i)\|\nabla\hat{i}\|dxdy\\ &+\lambda_4\int_\Omega(r-i+l)^2dxdy\\ &+\lambda_5\int_\Omega(I-I_0\ \log\ I)^2. \end{aligned}\tag{8}$$

The above-mentioned minimization problem can be converted into the following three subproblems.

r-subproblem:

$$\begin{aligned}\min_r\{E(r)\} = &\lambda_1\int_\Omega W(r)\|\nabla\hat{r}\|dxdy\\ &+\lambda_2\int_\Omega(\exp(r)-1/2)^2dxdy\\ &+\lambda_4\int_\Omega(r-i+l)^2dxdy.\end{aligned}\tag{9}$$

i-subproblem:

$$\begin{aligned}\min_i\{E(i)\} = &\lambda_3\int_\Omega redW(i)\|\nabla\hat{i}\|dxdy\\ &+\lambda_4\int_\Omega(r-i+l)^2dxdy\\ &+\lambda_5\int_\Omega(I-I_0\ \log\ I)^2dxdy.\end{aligned}\tag{10}$$

l-subproblem:

$$\begin{aligned}\min_l\{E(l)\} = &\int_\Omega\|\nabla l\|_2^2dxdy\\ &+\lambda_4\int_\Omega(r-i+l)^2dxdy.\end{aligned}\tag{11}$$

These subproblems are effectively solved using the split-Bregman algorithm. According to this, a constraint $d=\nabla\hat{r}$ is added in to the subproblem in (9) along with a new auxiliary variable b_1. The new subproblem under the above-mentioned modification amounts to

$$\begin{aligned}\min_r\{E(r)\} = &\lambda_1 W(r)\|d\|\\ &+\lambda_2(\exp(r)-1/2)^2\\ &+\lambda_4(r-i+l)^2\\ &+\lambda\|d-\nabla\hat{r}-b_1\|_2^2.\end{aligned}\tag{12}$$

For (10), a constraint $p=\nabla\hat{i}$ and an auxiliary variable b_2 is added to form the minimization problem as follows:

$$\begin{aligned}\min_i\{E(i)\} = &\lambda_3 W(i)\|p\|\\ &+\lambda_4(r-i+l)^2\\ &+\lambda_5(I-I_0\ \log\ I)^2\\ &+\alpha\|p-\nabla\hat{i}-b_2\|_2^2.\end{aligned}\tag{13}$$

Equation (12) can be split into $r,\ d$, and b_1 subproblems as follows:

$$\begin{aligned}r^{k+1} = \min_r\big\{&\lambda_2(\exp(r)-1/2)^2+\lambda_4(r-i+l)^2\\ &+\lambda\|d-\nabla\hat{r}-b_1^k\|_2^2\big\}\end{aligned}\tag{14}$$

$$d^{k+1} = \min_r\big\{\lambda_1 W(r)\|d\|+\lambda\|d-\nabla\hat{r}-b_1^k\|_2^2\big\}\tag{15}$$

and

$$b_1^{k+1} = b_1^k+(\nabla\hat{r}-d^{k+1}).\tag{16}$$

Similarly, (13) can be split into $i,\ p$, and b_2 subproblems as follows:

$$\begin{aligned}i^{k+1} = \min_r\big\{&\lambda_5(I-I_0\ \log\ I)^2+\lambda_4(r-i+l)^2\\ &+\alpha\|p-\nabla\hat{i}-b_2^k\|_2^2\Big\}\end{aligned}\tag{17}$$

$$p^{k+1} = \min_p\Big\{\lambda_3 W(i)\ \|p\|+\alpha\|p-\nabla\hat{i}-b_2^k\|_2^2\Big\}\tag{18}$$

and

$$b_2^{k+1} = b_2^k+(\nabla\hat{i}-p^{k+1}).\tag{19}$$

Euler–Lagrange derivative of (14) is evaluated as

$$\begin{aligned}\lambda_2(\exp(r)\ (\exp(r)-1/2))+\lambda_4(r-i+l)\\ +\lambda\nabla.(d-\nabla\hat{r}-b_1^k)=0.\end{aligned}\tag{20}$$

This can be solved effectively in the Fourier domain.[1]

[1]

$$r^{k+1} = F^{-1}\left\{\frac{\lambda_4 F(i-l)-\lambda_2 F((\exp(r)\ (\exp(r)-1/2)))-\lambda F(\nabla.(d-\nabla\hat{r}-b_1^k))}{\lambda_4}\right\}\tag{21}$$

where F and F^{-1} represent discrete Fourier transform (DFT) and its inverse, i.e., $y(m)=F(x(n))=\sum_{n=0}^{N-1}x(n)e^{-j\frac{2\pi}{N}mn}$ and $x(n)=F^{-1}(y(m))=\frac{1}{N}\sum_{m=0}^{N-1}y(m)e^{j\frac{2\pi}{N}mn}$.

Algorithm 1: Algorithm to Implement the Method.

Input $I_0 \leftarrow$ Low contrast and noisy Digital image of size $M \times N$

Output Enhanced and Restored Digital image I of size $M \times N$

Initialize[2] $k = 1, \epsilon = 0.0001, \lambda = 3.8, \lambda_2 = 6, \lambda_4 = 800, \lambda_5 = 0.001, \alpha = 0.8, d^1 = [0], b_1^1 = [0], p^1 = [0], b_2^1 = [0], i^1 = [\log(I_0)], l^1 = [\max(i^1)]$, and $r^1 = [(l^1 - i^1)]$

while do $\|i^{k+1} - i^k\|/\|i^{k+1}\| < \epsilon$

  Given $i^k, l^k$and r^k find r^{k+1} using (21)

  Update d^{k+1} using shrink operator as in (25)

  Update b_1^{k+1} using (27)

  Given $i^k, l^k, r^k$and I_0 solve (23) to get i^{k+1}

  update p^{k+1} using shrink operator as in (26)

  update b_2^{k+1} using (28)

  Given $i^k$and r^k find l^{k+1} using (30)

end while

update I as exponential of $(l + r)$

Euler–Lagrange derivative of (17) is as given as

$$\lambda_5(I - I_0) + \lambda_4(r - i + l) + \alpha\nabla.(p - \nabla\hat{i} - b_2^k) = 0. \quad (22)$$

The problem stated above is solved effectively in the Fourier domain as

$$i^{k+1} = F^{-1}\left\{\frac{\lambda_5 F(I_0) - \lambda_4 F(r + l) - \alpha F(\nabla.(p - \nabla\hat{i} - b_2^k))}{F((\lambda_5 \frac{I}{\hat{i}}) - \lambda_4)}\right\}. \quad (23)$$

The d and p subproblems in (15) and (18) can be solved by using $shrink$ function which is defined as

$$shrink(x, \theta) = \frac{x}{|x|}\max(|x| - \theta, 0). \quad (24)$$

Hence, these subproblems can be rewritten as follows (assumes $\lambda_1 = 1$ and $\lambda_3 = 1$):

$$d^{k+1} = shrink\left(\nabla\hat{r} + b_1^k, \frac{W(r)}{\lambda}\right) \quad (25)$$

$$p^{k+1} = shrink\left(\nabla\hat{i} + b_2^k, \frac{W(i)}{\alpha}\right). \quad (26)$$

Auxiliary variables b_1 and b_2 are updated using

$$b_1^{k+1} = b_1^k + (\nabla\hat{r} - d^{k+1}) \quad (27)$$

$$b_2^{k+1} = b_2^k + (\nabla\hat{i} - p^{k+1}). \quad (28)$$

Finally, the optimization problem in (11) is solved by taking the Euler–Lagrange derivative which derives

$$\Delta l + \lambda_4(r - i + l) = 0. \quad (29)$$

[2]All initializations in [] represent matrices of size $M \times N$, e.g., [0] denotes an $M \times N$ matrix initialized with zeros

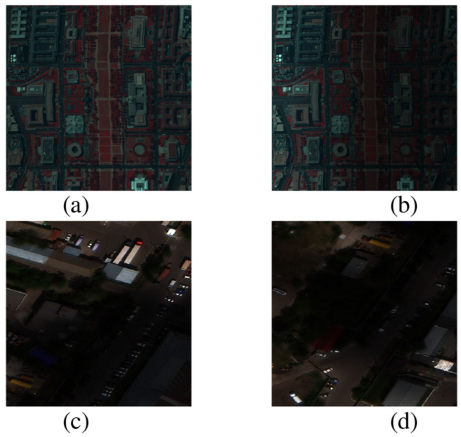

Fig. 1. Test images used: (a) original hyperspectral image of Washington DC (HYDICE, 191 spectral bands, spatial resolution: 2.8 m, pixels used: 307 × 307, bands used: 60, 27, and 17), courtesy MultiSpec by Purdue University; (b) vertically contrast degraded image after applying mask; (c) and (d) original WorldView-3 satellite images at 0.3 m ground sample distance, courtesy xView dataset [23].

The above-mentioned expression is solved in the Fourier domain as

$$l^{k+1} = F^{-1}\left\{\frac{\lambda_4 F(i - r)}{F(\lambda_4 + \Delta)}\right\}. \quad (30)$$

The overall algorithm of the process is highlighted as follows.

IV. Experimental Study

The testing of various models is done using a large set of images falling under the category of hyperspectral and aerial imagery. However, to maintain the brevity in explanation, only a subset of them, i.e., three synthetically noisy images (two xView satellite images and Washington DC, see Fig. 1), and two original noisy data (Pines and Jasper Ridge), have been used for demonstrating the results. Nevertheless, the performances of the methods to the other test images are observed to follow the pattern exhibited by the demonstrated ones. Nonuniformly illuminated and Poisson-noisy versions of these test images are used as the input to the system, see Fig. 1 for the original images. Fig. 1(a) shows the original Washington DC false-color image, which is converted to a vertically contrast degraded image by using a mask, and the resultant image is given in Fig. 1(b). Fig. 1(c) and (d) is the originally contrast degraded satellite images. Poisson noise of peak 100 is used to degrade all these test images synthetically; corresponding noisy images are given in Figs. 2(a), 3(a), and 4(a). The performance of various comparative models for real noisy input images are shown in Figs. 5 and 6. The different parameter values used for the experiments are $\lambda = 3.8, \lambda_2 = 6, \alpha = 0.8, \lambda_4 = 800, \lambda_5 = 0.001$ and for the hyperspectral images which are prone to more contrast degradation, the value of the parameter λ_2 is raised to 7.5. Among the parameters mentioned above, λ and λ_2 are specifically for processing the reflectance part of the image. Similarly, α and λ_5 controls the regularity and fidelity of the intensity data. λ_4 signifies a global fidelity term. The parameter λ is observed to control the diffusion of reflectance part of

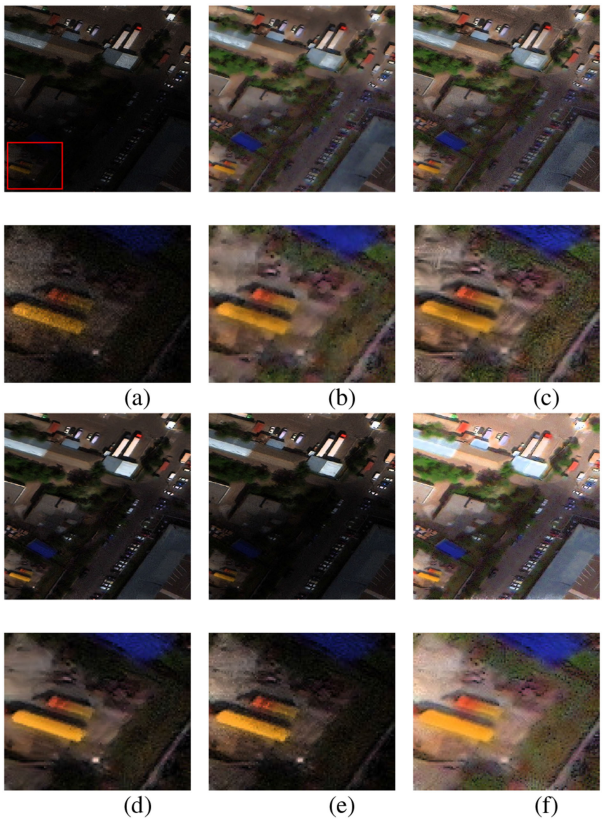

Fig. 2. xView image 1 with Poisson noise: (a) input image; (b) restored using Fast TV+CLAHE [25]; (c) restored using NLTV+CLAHE [26]; (d) restored using NLTVR+NLTV [18]; (e) restored using PVM+NLTV [19]; and (f) restored using the proposed method.

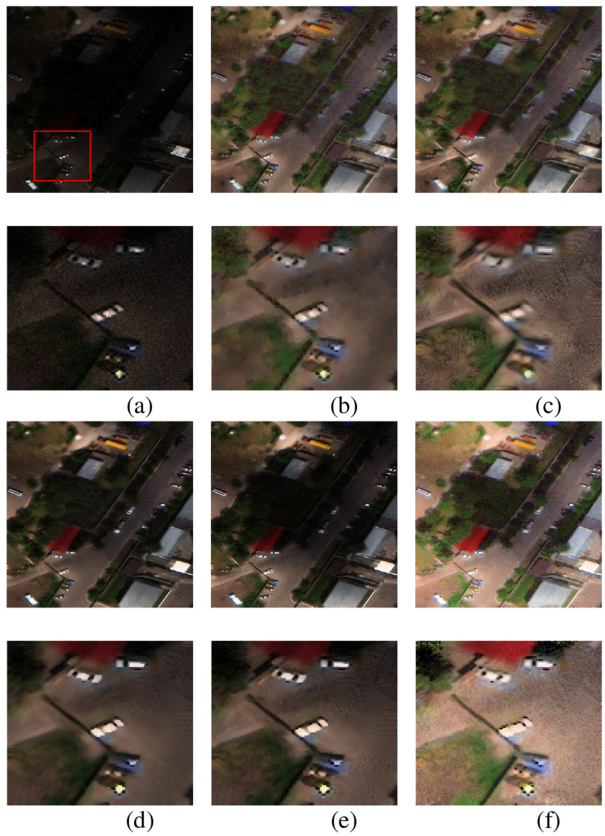

Fig. 3. xView image 2 with Poisson: (a) input image; (b) restored using Fast TV+CLAHE [25]; (c) restored using NLTV+CLAHE [26]; (d) restored using NLTVR+NLTV [18]; (e) restored using PVM+NLTV [19]; and (f) restored using the proposed method.

the data. The reflectance includes the textures and other fine details. Therefore, the value of this one is chosen to ensure the tradeoff between smoothing and preserving details. Throughout the experiment, we have used a fixed value for this term to retain the natural textured effect on the image. Upon an increase in the peak value of the noise, the parameter α has to be increased subsequently to maintain the restoration efficiency of the model. However, a very high value for this parameter may deteriorate the edge-preservation capability of the model under consideration. To address this issue, the value of λ_5 is chosen appropriately to check the loss of information in the course of evolution. The term associated with the parameter λ_5 is the data-fidelity term derived based on the distribution characteristics of the noise (the noise is assumed as an output of a Poisson process). For a very low peak noise, the λ_5 value should be slightly higher.

The denoising ability of the system is categorically demonstrated using the state-of-the-art Poisson denoising models such as Fast TV [25] and NLTV (nonlocal TV) [26]. Though the restoration methods considered for the comparison do not possess an enhancement capacity by themselves unlike the proposed model, we have associated an additional enhancement characteristic to them (FAST TV+CLAHE, NLTV+CLHE, etc.) in order to make them in line with the proposed model for the sake of comparative study. The enhancement achieved by the system is also compared with the recent retinex-based enhancement methods such as nonlocal TV retinex (NLTVR) [18] and perceptually inspired variational model (PVM) for remote sensing [19]. Since we are proposing a nonlocal retinex framework, in order to justify the comparative results of the other methods, we have combined the retinex based enhancement methods with NLTV denoising method to form the NLTVR+NLTV and PVM+NLTV.

In addition to the visual comparisons, a quantitative study has been carried out using various quality metrics such as AG (average gradient) [27], NIQE (naturalness image quality evaluator) [28], GCF (global contrast factor) [30], entropy [31], and visual descriptors [32] e (rate of new visible edges), $\bar{r}$ (quality of contrast restoration), and σ (number of saturated pixels).

The resultant images of various comparative methods are portrayed in Figs. 2–4. Although most of the methods considered herein for the comparative study perform fairly well as far as denoising is concerned, the NLTVR+NLTV method performs slightly better when both denoising and enhancement are considered at once. Nonetheless, the proposed strategy exhibits a profound quality in the visual representations. The zoomed-in portions of the image duly justify the detail-preserving capabilities of the proposed model. In Fig. 3, the contrast enhancement obtained by the proposed method is promising, and the corresponding enlarged image also shows the denoising capability

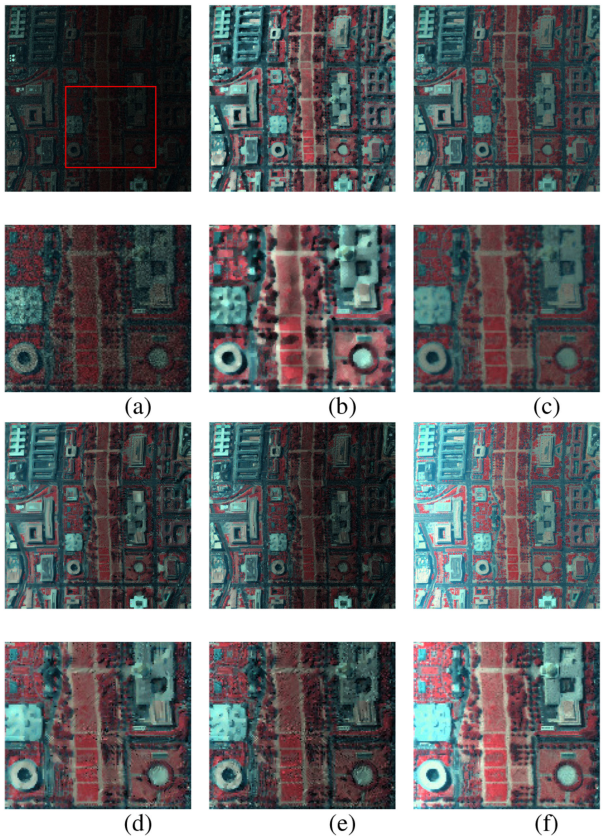

Fig. 4. Washington DC image with Poisson: (a) input image; (b) restored using Fast TV+CLAHE [25]; (c) restored using NLTV+CLAHE [26]; (d) restored using NLTVR+NLTV [18]; (e) restored using PVM+NLTV [19]; and (f) restored using the proposed method.

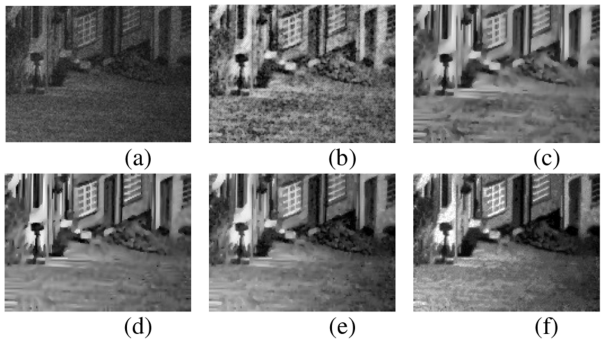

Fig. 5. Optical image with Poisson noise peak = 30: (a) input image; (b) restored using Fast TV+CLAHE [25]; (c) restored using NLTV+CLAHE [26]; (d) restored using NLTVR+NLTV [18]; (e) restored using PVM+NLTV [19]; and (f) restored using the proposed method.

of the system. As noticeable from Fig. 4, the NLTVR+NLTV, PVM+NLTV, and the proposed method apparently preserve uniform illumination in the data, and the output appears more natural. Further, analyzing the enlarged portions of the restored outputs, the proposed model is observed to preserve textures and details better than the other ones.

Table I gives the comparison of different denoising methods on the basis of AG and NIQE values. NIQE depicts the naturalness of the restored image and AG measures the quality of the

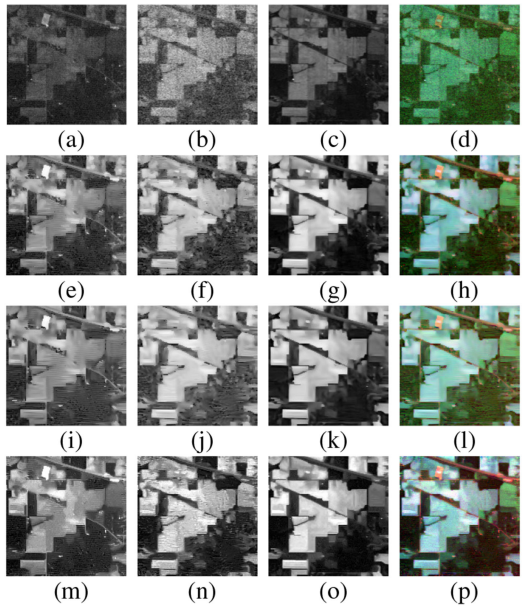

Fig. 6. Results on low-contrast noisy bands of Indian Pines (AVIRIS, 145×145 pixels, 224 spectral reflectance bands, wavelength range: 0.4–2.5 $\times 10^{-6}$ m), courtesy MultiSpec : (a) input low-contrast noisy Band 3; (b) input low-contrast noisy Band 110; (c) input low-contrast noisy Band 204; (d) noisy False color image; PVM+NLTV: (e) Band 3 restored; (f) Band 110 restored; (g) Band 204 restored; (h) restored false color image; NLTVR+NLTV: (i) Band 3 restored; (j) Band 110 restored; (k) Band 204 restored; (l) restored false color image; proposed: (m) Band 3 restored; (n) Band 110 restored; (o) Band 204 restored; and (p) restored false color image.

image. A high value of NIQE indicates a low performance in terms of denoising. As the value decreases, the restoration gets improved. Whereas a high value of AG implies better spatial resolution [27]. According to Table I, the FastTV+CLAHE is giving comparable performances in some synthetically noisy inputs, and the performance of PVM+NLTV is also on par with the proposed method in original noisy data (Pines, Jasper Ridge); however, the proposed method displays consistently better performance for all images. The measures in Table I check the naturalness of the image and its clarity; hence, the higher performance here implies better restoration. To measure the quality of detail preservation, we have evaluated the discrete entropy of the image. Generally, entropy measures information content; hence, higher entropy values imply the presence of more details in the filtered image. Table II gives a comparison of discrete entropy values. As inferred from this table, the detail-preservation capability of the proposed strategy is more dominant than all the other methods under study. Table II also shows the comparison of GCF among different methods. It is a global measure of contrast, and it is stated to be more close to the human perception of contrast [30]. It operates in different scales of resolution to get local contrast information and a weighted average of which will be calculated as GCF. A high value of this measure implies an improvement in the contrast and high visibility of the details. According to Table II, the proposed methodology has a higher GCF for all images. Table III describes the visual descriptors obtained for different methods. The e and $\bar{r}$ values are high if the restored results have high visibility and

TABLE I
AG AND NIQE EVALUATED FOR VARIOUS METHODS

Images	Quality metrics	Fast TV+CLAHE [25]	NLTV+CLAHE [26]	NLTVR+NLTV [18]	PVM+NLTV [19]	Proposed method
Washington DC	AG	48.6268	38.9858	45.2348	41.4343	**50.0104**
	NIQE	5.7783	5.4592	6.2676	6.2449	**5.3555**
xView 1	AG	22.2802	30.3130	24.4006	21.0895	**31.8546**
	NIQE	6.1672	6.6492	6.6822	6.7088	**6.1458**
xView 2	AG	22.7537	26.7697	21.8139	20.9387	**53.6950**
	NIQE	5.2839	6.6844	5.1235	5.1579	**5.1215**
Pines	AG	50.4822	51.7613	51.1983	50.8462	**59.2906**
	NIQE	39.8003	39.8643	39.8002	39.7995	**39.7994**
Jasper Ridge	AG	34.8662	38.7902	38.8006	34.1701	**38.9568**
	NIQE	38.4545	39.8014	39.8006	**39.8001**	**39.8001**

The bold entries in the table denote the optimal values for the corresponding measure.

TABLE II
GCF AND EM EVALUATED FOR VARIOUS METHODS

Images	Quality metrics	Fast TV+CLAHE [25]	NLTV+CLAHE [26]	NLTVR+NLTV [18]	PVM+NLTV [19]	Proposed method
Washington DC	GCF	6.8124	6.1452	6.6792	6.6731	**6.8423**
	EM	7.4730	6.9371	7.1578	7.1176	**7.6097**
xView 1	GCF	5.7280	6.1470	7.2725	7.1195	**7.7424**
	EM	6.9791	6.1294	6.6822	6.4970	**7.6940**
xView 2	GCF	5.9825	6.5800	7.2038	7.5713	**7.6093**
	EM	7.0026	7.1094	6.8778	6.8838	**7.6475**
Pines	GCF	7.6881	6.5214	6.5945	8.4802	**8.5215**
	EM	7.6044	7.6391	7.7819	7.7722	**7.8388**
Jasper Ridge	GCF	7.0671	6.0351	6.1817	7.5104	**8.7325**
	EM	7.1104	7.3915	7.6713	7.6708	**7.6730**

The bold entries in the table denote the optimal values for the corresponding measure.

TABLE III
VISUAL DESCRIPTORS EVALUATED FOR VARIOUS METHODS

Images	Quality metrics	Fast TV+CLAHE [25]	NLTV+CLAHE [26]	NLTVR+NLTV [18]	PVM+NLTV [19]	Proposed method
Washington DC	e	-0.1895	-0.1523	-0.1597	-0.1597	**-0.1521**
	$\bar{\mathrm{r}}$	3.554	2.5294	2.8437	2.3719	**3.8885**
	σ	0.0130	0.0116	0.0485	0.0134	**0.0109**
xView 1	e	-0.5065	-0.2536	-0.2963	-0.1738	**-0.1729**
	$\bar{\mathrm{r}}$	2.4125	2.8910	1.9283	1.4186	**3.3906**
	σ	**0.00**	**0.00**	0.0139	0.1466	**0.00**
xView 2	e	-0.5056	-0.2818	-0.3680	-0.2794	**-0.2426**
	$\bar{\mathrm{r}}$	2.9659	2.7704	2.1440	1.7779	**3.2680**
	σ	**0.00**	**0.00**	0.0763	0.0025	**0.00**
Pines	e	0.0154	0.0156	0.0101	0.0156	**0.0188**
	$\bar{\mathrm{r}}$	1.4931	1.4714	1.5605	1.4702	**1.7049**
	σ	0.0183	0.0250	0.0110	0.0146	**0.0101**
Jasper Ridge	e	-0.0384	-0.0325	-0.0336	-0.0368	**-0.0273**
	$\bar{\mathrm{r}}$	1.1681	1.1643	1.2513	1.1797	**1.2625**
	σ	0.5030	0.6110	0.1500	0.5533	**0.0121**

The bold entries in the table denote the optimal values for the corresponding measure.

TABLE IV
TIME TAKEN BY DIFFERENT METHODS IN SECONDS

Images	Fast TV+CLAHE [25]	NLTV+CLAHE [26]	NLTVR+NLTV [18]	PVM+NLTV [19]	Proposed method
Washington DC	5.4706	6.1788	26.5439	7.6272	**3.3718**
xView 1	6.0304	8.9574	163.0553	11.3595	**4.0991**
xView 2	6.0094	8.9712	129.1649	11.2597	**4.1921**

The bold entries in the table denote the optimal values for the corresponding measure.

σ is less when the number of saturated pixels is less. In light of these results, we observe that the proposed model outperforms the other ones. Finally, Table IV includes the time taken by different algorithms for restoration. As evident from this table, the proposed method converges faster.

In addition to the remote-sensing images, the performance on natural image (optical image) is demonstrated in Fig. 5, and it is observed that the denoising and enhancement obtained by the proposed algorithm are on par with the other methods. The results obtained on real noisy input images are represented in Figs. 6 and 7. The noisy bands (3, 110, 204), Indian Pines dataset (http://lesun.weebly.com/hyperspectral-data-set.html), and (4, 107, 153), Jasper Ridge dataset have been used here for the evaluation. The performance of comparing algorithms on each band is shown in the subfigures. The first row of the figure is showing all noisy bands and the last column in this figure represents the false colour image formed using all these bands. In case of a regular RGB image, the proposed algorithm can be applied in each band as depicted herein but this leads to color distortions in the input data; in order to reduce this colour discrepancy, operation in the HSV domain is recommended.

As inferred from the experimental study, the proposed method is prominent in preserving textures and other details present in the input while denoising and enhancing the data.

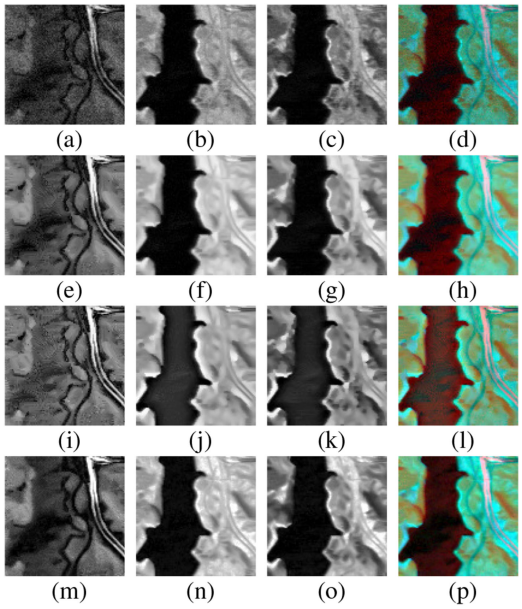

Fig. 7. Results on low-contrast noisy bands of Japser Ridge [24] (subimage of 100×100 pixels, 224 bands, wavelength range: 380–2500 nm): (a) input low-contrast noisy Band 4; (b) input low-contrast noisy Band 107; (c) input low-contrast noisy Band 153; (d) noisy False color image; PVM+NLTV: (e) Band 4 restored; (f) Band 107 restored; (g) Band 153 restored; (h) restored false color image; NLTVR+NLTV: (i) Band 4 restored; (j) Band 107 restored; (k) Band 153 restored; (l) restored false color image; proposed: (m) Band 4 restored; (n) Band 107 restored; (o) Band 153 restored; and (p) restored false color image.

V. Conclusion

In this article, a perceptually inspired image restoration model is proposed for restoring and enhancing aerial/satellite images. The intensity inhomogeneity in these images are taken care of while restoring them from noise intervention. The presence of a data-correlated noise along with contrast inhomogeneity has been addressed in this work. The nonlocal framework employed here efficiently preserves the image features. Compared to other popular methods, the proposed technique shows both denoising and enhancing capability. The results perceived from the image representations and numerical quantifications are in favor of the proposed strategy. In the future, this method can be further expanded to handle Poisson–Gaussian mixed noise.

Appendix A
MAP Estimator for Poisson Noise

In this section, a MAP estimation of the Poisson PDF is detailed. According to the Bayes rule

$$P(x|y) = \frac{P(y|x)P(x)}{P(y)} \tag{31}$$

where x and y represent the random variables and $P(x|y)$ represents the conditional probability, i.e., probability of x given y. In the imaging domain, it represents $P(I|I_0)$, where I and I_0 are the original and distorted image, respectively.

MAP estimator maximizes the posterior probability $P(I|I_0)$ which takes the form (thanks to Bayesian formulation)

$$\min_I \Big\{ P(I|I_0) \Big\} = \max_I \Big\{ (P(I_0|I))\ P(I) \Big\}. \tag{32}$$

In the above-mentioned equation, $P(I)$ is known as prior probability and $P(I_0)$ is a constant which does not affect the minimization process (therefore, it is omitted in further steps). The maximization problem in (32) is the same as the minimization of its $-\log$ likelihood, which takes the form

$$\min_I \Big\{ -\log(P(I|I_0)) \Big\} = \min_I \Big\{ -\log(P(I_0|I)) - \log(P(I)) \Big\}. \tag{33}$$

In case of Poisson distribution $p(I_0|I) = \frac{e^{-I}\, I^{I_0}}{I_0!}$ and assuming a Gibb's prior $P(I) = e^{(-\lambda/2\phi(I))}$, the minimization problem will be as follows [26]:

$$\min_u \Big\{ \sum I - I_0\ \log\ I + \lambda\ \phi(I) \Big\}. \tag{34}$$

In the above functional, $\phi(.)$ denotes regularization prior.

References

[1] H. Demirel, C. Ozcinar, and G. Anbarjafari, "Satellite image contrast enhancement using discrete wavelet transform and singular value decomposition," *IEEE Geosci. Remote Sens. Lett.*, vol. 7, no. 2, pp. 333–337, Apr. 2010.
[2] H.-J. Kwak and G.-T. Park, "Image contrast enhancement for intelligent surveillance systems using multi-local histogram transformation," *J. Intell. Manuf.*, vol. 25, no. 2, pp. 303–318, Apr. 2014.
[3] H. Ibrahim and N. S. P. Kong, "Brightness preserving dynamic histogram equalization for image contrast enhancement," *IEEE Trans. Consum. Electron.*, vol. 53, no. 4, pp. 1752–1758, Nov. 2007.
[4] T. Arici, S. Dikbas, and Y. Altunbasak, "A histogram modification framework and its application for image contrast enhancement," *IEEE Trans. Image Process.*, vol. 18, no. 9, pp. 1921–1935, Sep. 2009.
[5] S. C. Huang, F. C. Cheng, and Y. S. Chiu, "Efficient contrast enhancement using adaptive gamma correction with weighting distribution," *IEEE Trans. Image Process.*, vol. 22, no. 3, pp. 1032–1041, Mar. 2013.
[6] H. Demirel, G. Anbarjafari, and M. N. S. Jahromi, "Image equalization based on singular value decomposition," in *Proc. IEEE 23rd Int. Symp. Comput. Inf. Sci.*, 2008, pp. 1–5.
[7] X. Fu, J. Wang, D. Zeng, Y. Huang, and X. Ding, "Remote sensing image enhancement using regularized-histogram equalization and DCT," *IEEE Geosci. Remote Sens. Lett.*, vol. 12, no. 11, pp. 2301–2305, Nov. 2015.
[8] J. Liu, C. Zhou, P. Chen, and C. Kang, "An efficient contrast enhancement method for remote sensing images," *IEEE Geosci. Remote Sens. Lett.*, vol. 14, no. 10, pp. 1715–1719, Oct. 2017.
[9] E. Lee, S. Kim, W. Kang, D. Seo, and J. Paik, "Contrast enhancement using dominant brightness level analysis and adaptive intensity transformation for remote sensing images," *IEEE Geosci. Remote Sens. Lett.*, vol. 10, no. 1, pp. 62–66, Jan. 2013.
[10] J. H. Jang, S. D. Kim, and J. B. Ra, "Enhancement of optical remote sensing images by subband-decomposed multiscale retinex with hybrid intensity transfer function," *IEEE Geosci. Remote Sens. Lett.*, vol. 8, no. 5, pp. 983–987, Sep. 2011.
[11] G. Zhang, Q. Chen, and Q. Sun, "Illumination normalization among multiple remote-sensing images," *IEEE Geosci. Remote Sens. Lett.*, vol. 11, no. 9, pp. 1470–1474, Sep. 2014.
[12] B. Rasti, P. Scheunders, P. Ghamisi, G. Licciardi, and J. Chanussot, "Noise reduction in hyperspectral imagery: Overview and application," *Remote Sens.*, vol. 10, no. 3, 2018, Art. no. 482.
[13] E. H. Land and J. J. McCann, "Lightness and retinex theory," *J. Opt. Soc. Amer.*, vol. 61, no. 1, pp. 1–11, 1971.
[14] E. H. Land, "The retinex theory of color vision," *Sci. Amer.*, vol. 237, no. 6, pp. 108–128, 1977.

[15] E. H. Land, "Recent advances in the retinex theory and some implications for cortical computations: Color vision and natural image," *Proc. Nat. Acad. Sci. USA*, vol. 80, no. 16, pp. 5163–5169, 1983.
[16] R. Kimmel, M. Elad, D. Shaked, R. Keshet, and I. Sobel, "A variational framework for retinex," *Int. J. Comput. Vis.*, vol. 52, pp. 7–23, 2003.
[17] M. K. Ng and W. Wang, "A total variation model for retinex," *SIAM J. Imag. Sci.*, vol. 4, pp. 345–365, 2014.
[18] D. Zosso, G. Tran, and S. Osher, "Non-local retinex—A unifying framework and beyond," *SIAM J. Imag. Sci.*, vol. 8, pp. 787–826, 2015.
[19] H. Li, L. Zhang, and H. Shen, "Perceptually inspired variational method for the uneven intensity correction of remote sensing images," *IEEE Trans. Geosci. Remote Sens.*, vol. 50, no. 8, pp. 3053–3065, Aug. 2012.
[20] X. Lan, H. Shen, L. Zhang, and Q. Yuan, "A spatially adaptive retinex variational model for the uneven intensity correction of remote sensing images," *Signal Process.*, vol. 101, pp. 19–34, 2014.
[21] G. Guy and O. Stanley, "Nonlocal operators with applications to image processing," *Multiscale Model. Simul.*, vol. 7, no. 3, pp. 1005–1028, 2008.
[22] Shen J, "On the foundations of vision modeling I. Weber's law and Weberized TV restoration," *Physica D*, vol. 175, pp. 241–251, 2003.
[23] D. Lam *et al.*, "xView: Objects in context in overhead imagery," *CoRR*, 2018, *arXiv:1802.07856*.
[24] F. Zhu, Y. Wang, S. Xiang, B. Fan, and C. Pan, "Structured sparse method for hyperspectral unmixing," *ISPRS J. Photogramm. Remote Sens.*, vol. 88, pp. 101–118, 2014.
[25] W. Wang and C. He, "A fast and effective method for a Poisson denoising model with total variation," *IEEE Signal Process. Lett.*, vol. 24, no. 3, pp. 269–273, Mar. 2017.
[26] S. H. Kayyar and P. Jidesh, "Non-local total variation regularization approach for image restoration under a Poisson degradation," *J. Modern Opt.*, vol. 65, no. 19, pp. 2231–2242, 2018.
[27] S. Li, Z. Yang, and H. Li, "Statistical evaluation of no-reference image quality assessment metrics for remote sensing images," *ISPRS Int. J. Geo-Inf.*, vol. 6, no. 5, Apr. 2017, Art. no. 133.
[28] A. Mittal, R. Soundararajan, and A. C. Bovik, "Making a completely blind image quality analyzer," *IEEE Signal Process. Lett.*, vol. 20, no. 3, pp. 209–212, Mar. 2013.
[29] F. Timischl, "The contrast-to-noise ratio for image quality evaluation in scanning electron microscopy," *Scanning*, vol. 37, pp. 54–62, 2015.
[30] K. Matkovic, L. Neumann, A. Neumann, and T. Psik, "Global contrast factor—A new approach to image contrast," in *Proc. Comput. Aesthetics*, May 2005, pp. 159–168.
[31] V. Karathanassi, P. Kolokousis, and S. Ioannidou, "A comparison study on fusion methods using evaluation indicators," *Int. J. Remote Sens.*, vol. 28, pp. 2309–2341, 2007.
[32] N. Hautière, J.-P. Tarel, D. Aubert, and E. Dumont, "Blind contrast enhancement assessment by gradient ratioing at visible edges," *Image Anal. Stereology*, vol. 27, no. 2, pp. 87–95, 2008.

I. P. Febin (Student Member, IEEE) received the B.Tech. degree in information technology from the Rajagiri School of Engineering and Technology, Ernakulam, India, in 2010, and the M.Tech. degree in computer science with specialization in image processing from Government Model Engineering College, Kochi, India, in 2016.

She was formerly an Assistant Systems Engineer with Tata Consultancy Services Ltd. She is currently a Senior Research Fellow with the Department of Mathematical and Computational Sciences, National Institute of Technology Karnataka, Surathkal, India. Her research interests include image restoration, pattern recognition, and computer vision.

P. Jidesh (Senior Member, IEEE) received the Ph.D. degree from the Department of Mathematical and Computational Sciences, National Institute of Technology Karnataka, Surathkal, India.

Since January 2009, he has been with the same department, where he is currently an Assistant Professor. He has authored or coauthored several papers in reputed international journals and conferences. His research interests include mathematical imaging, graph image processing, and data compression.

A. A. Bini received the Ph.D. degree from the Department of Electronics and Communication Engineering, National Institute of Technology Karnataka, Surathkal, India, in 2015.

She is presently an Assistant Professor with the Indian Institute of Information Technology, Kottayam, India. She has authored or coauthored several papers in reputed journals. Her research interests include signal processing, image processing, communication engineering, etc.